

An integrated observation dataset of the hydrological-thermal deformation in permafrost slopes and engineering infrastructure in the Qinghai-Tibet Engineering Corridor

Lihui Luo^{1,2,3}, Yanli Zhuang^{1,3}, Mingyi Zhang^{1,2,3}, Zhongqiong Zhang^{2,3}, Wei Ma^{2,3},
Wenzhi Zhao^{1,3}, Lin Zhao⁴, Li Wang⁵, Yanmei Shi⁶, Ze Zhang^{2,3}, Quntao Duan^{1,3},
Deyu Tian¹, Qingguo Zhou⁷

¹Northwest Institute of Eco-Environment and Resources, Chinese Academy of Sciences, Lanzhou 730000, China

²State Key Laboratory of Frozen Soils Engineering, Northwest Institute of Eco-Environment and Resources, Chinese Academy of Sciences, Lanzhou 730000, China

³University of Chinese Academy of Sciences, Beijing 100049, China

⁴Cryosphere Research Station on Qinghai-Xizang Plateau, Northwest Institute of Eco-Environment and Resources, Chinese Academy of Sciences, Lanzhou 730000, China

⁵Qinghai Institute of Meteorological Science, Xining 810001, China

⁶32016 PLA Troops, Lanzhou 730000, China

⁷School of Information Science and Engineering, Lanzhou University, Lanzhou 730000, China

Correspondence: Lihui Luo (luolh@lzb.ac.cn)

Abstract. Across the Qinghai-Tibet Plateau (QTP) there is a narrow engineering corridor with widely distributed slopes, called the Qinghai-Tibet Engineering Corridor (QTEC), where a variety of important infrastructures are concentrated. These facilities are transportation routes for people, materials, energy, etc., from mainland China to Tibet. From Golmud to Lhasa, the engineering corridor covers 632 km of permafrost containing the densely occurring Qinghai-Tibet Railway and Highway as well as power/communication towers. Slope failure in permafrost regions, caused by permafrost degradation, ground ice melting, etc., affects the engineering construction and permafrost environments in the QTEC. We implement a variety of sensors to monitor the hydrological-thermal deformation between permafrost slopes and permafrost engineering projects in the corridor. In addition to soil temperature and moisture sensors, the global navigation satellite system (GNSS), terrestrial laser scanning (TLS), and unmanned aerial vehicles (UAVs) were adopted to monitor the spatial distribution and changes in thermal deformation. An integrated dataset of hydrological-thermal deformation in permafrost engineering and slopes in the QTEC from the 1950s to ~~2019~~2020, including meteorological and ground observations, TLS point cloud data, and RGB and thermal infrared (TIR) images, can be of great value for estimating the hydrological-thermal impact and stability between engineering and slopes under the influence of climate change and engineering disturbance. The dataset and code were uploaded to the Zenodo repository and can be accessed through <https://zenodo.org/communities/qttec>, including meteorological and ground observations at <http://doi.org/10.5281/zenodo.4588099> (Luo et al., 2020d), TLS measurements at <http://doi.org/10.5281/zenodo.4588090> (Luo et al., 2020a), UAV RGB and TIR images at <http://doi.org/10.5281/zenodo.4686506> (Luo et al., 2020b), and R code for permafrost indices and visualization at <http://doi.org/10.5281/zenodo.4686141> (Luo et al., 2020c).

Permafrost is frozen soil or rock containing ice, and organic material remains at or below 0 °C for at least two consecutive years and occurs mostly in the Northern Hemisphere, Alaska, and the Qinghai-Tibet Plateau (QTP) (Wang et al., 2018;Zhang et al., 1999). As a typical mountain permafrost region, permafrost slopes occur widely across the QTP. ~~Inevitably, much of the QTP infrastructure is built on these slopes (Luo et al., 2018c;Jin et al., 2008).~~ There exists a narrow engineering corridor on the QTP, where a variety of important infrastructures are concentrated, called the Qinghai-Tibet Engineering Corridor (QTEC) (Luo et al., 2018b;Zhang et al., 2015). These facilities are transportation routes for people, materials, energy, etc., from mainland China to Tibet, and the QTEC is several hundred meters to several kilometers wide. From Golmud to Lhasa across the QTP, more than 1120 km of the engineering corridor contains the densely occurring Qinghai-Tibet Highway (QTH), Golmud-Lhasa pipeline, Lanzhou-Xining-Lhasa fiber optic cable, Qinghai-Tibet Railway (QTR), and 440-kV Qinghai-Tibet DC networking system, which were completed and opened in 1954, 1977, 1997, 2006, and 2013, respectively (Jin et al., 2008). There are more than 6 major linear projects in the QTEC, covering 632 km of permafrost and approximately 550 km of continuous permafrost, with widely distributed slopes (Luo et al., 2018b). Inevitably, parts of these infrastructures are built on these slopes (Luo et al., 2018c;Jin et al., 2008).

Against the background of global climate change and increasing human activities, permafrost degradation is remarkable, resulting in an increase in the number of permafrost disasters (Huggel et al., 2010;Streletskiy et al., 2019;Bessette-Kirton and Coe, 2020;Patton et al., 2019). In engineering around permafrost slopes, permafrost disasters have widely occurred (Ma et al., 2006;Guo and Sun, 2015;Yu et al., 2020). Slope instability-type disasters tend to occur frequently, thereby causing direct or potential harm to the engineering projects in this region, which has become the main problem affecting the safe operation and service performance of these engineering projects while increasing the difficulty and cost of engineering maintenance (Niu et al., 2015;Wirz et al., 2015). Engineering in permafrost areas will inevitably destroy the surface energy and moisture balance, resulting in higher temperatures at the top of the permafrost (TTOP) and a lower permafrost table (Zhang et al., 2020;Liu et al., 2020;Zhao et al., 2020). Permafrost engineering occurs on slopes, which changes the circulation of surface and suprapermafrost water, causing thermal erosion (Han et al., 2019;Mu et al., 2018). Permafrost is affected not only by the construction and operation of engineering but also by the long-term heat impact of climate change (Wicky and Hauck, 2017;Gruber and Haeberli, 2007). In particular, high temperatures and highly ice-rich permafrost with a mean annual air temperature (MAAT) above -1.0 °C and an ice volume content higher than 25% are more sensitive to climate change and disturbances in engineering activities (Wu and Zhang, 2008;Patton et al., 2019). In the past 60 years, the MAAT of the seasonal and island permafrost areas along the QTEC has increased 0.3 to 0.5 °C, and the MAAT in the continuous permafrost area has increased 0.1 to 0.3 °C (Obu et al., 2019;Luo et al., 2018c;Wu et al., 2007). The QTP is a large-scale amplifier of global change, experiencing warming above the global average. If the air temperature rises to 2.6 °C, permafrost with a mean annual ground temperature (MAGT) higher than -1.0 °C will degrade to seasonal frozen soil after 50 years (Luo et al., 2018c;Wu et al., 2002). Furthermore, the permafrost slope in the freezing or/and thawing process is subject to frost heave or/and thawing subsidence,

which leads to deformation and even destruction of the foundation of engineering facilities, thereby affecting the normal use of these engineering facilities (Streletskiy et al., 2019; Yu et al., 2020; Ma et al., 2017). Warming of the climate and operation of permafrost projects around slopes have caused the ground temperature to rise. On ice-rich slopes, melting underground ice due to rising temperatures reduces the cohesion and angle of internal friction between the active layer and underground ice and becomes extremely unstable under the influence of gravity (Yuan et al., 2017). The locations of these slopes near permafrost engineering projects, such as railways and highways, thaw slumps, frost heaves, landslides, rockfalls, etc., may cause serious damage to permafrost engineering (Niu et al., 2015; Luo et al., 2018a).

The Chinese National Highway Network Plan, released in 2004, is aimed at building the Beijing-Lassa Expressway, which will be the only expressway to enter Tibet. The Beijing-Tibet Expressway will also be built within this narrow QTEC and will run parallel to or cross-positioned to the already crowded corridor (Ma et al., 2017). The interaction between the dense layout of various permafrost engineering facilities and permafrost slopes cannot be ignored. The stability and potential disaster of permafrost slopes constitute an area of increased interest of the international permafrost community, but studies on the spatiotemporal dynamics on unstable permafrost slopes in the QTEC are still lacking. A thorough understanding of the impact of a variety of permafrost engineering infrastructures (QTHs, QTRs, power/communication towers, etc.) that are densely distributed on or around permafrost slopes is lacking (Wang et al., 2020; Ma et al., 2019). Therefore, it is important to evaluate the interaction and influence between permafrost slopes and permafrost engineering by integrating hydrological-thermal deformation monitoring (Luo et al., 2018a).

Terrestrial laser scanning (TLS) with the global navigation satellite system (GNSS) was used to monitor the deformation of permafrost slopes (Luo et al., 2017; Arenson et al., 2016) and steep bedrock permafrost (Weber et al., 2019) to construct a high-resolution digital terrain model of the permafrost region (Boike et al., 2019). GNSS can be used as the datum point and control point of TLS, helping TLS point cloud data establish a georeferenced coordinate system and improving the accuracy of comparative analysis of multiple TLS data. Unmanned aerial vehicles (UAVs) can be equipped with visible digital, thermal infrared (TIR), and multispectral sensors. In addition to obtaining the topographic and landform features of the two frozen soil slopes, it can also estimate the spatial distribution of the ground surface temperature on permafrost slopes and evaluate the thermal influence of nearby engineering infrastructure (Luo et al., 2018a). UAVs can be used to monitor vegetation and terrain information in permafrost regions (Léger et al., 2019). Sluijs et al. (2018) also adopted UAVs to quantify the deformation of thaw slumps and to estimate the transfer volumes of sediment.

We provide an integrated dataset of the hydrological-thermal deformation covering permafrost engineering and slope areas in the QTEC ~~from 2014 to 2019.~~ In addition to using soil temperature and moisture sensors to monitor in situ hydrothermal changes, GNSS, TLS, and UAVs were also adopted to observe the spatial distribution of thermal deformation. This synthesis dataset for permafrost engineering and slopes includes measured air and ground temperatures and moisture ~~at depth intervals up to 2.6 m,~~ MAAT, MAGT, TLS point cloud data, and RGB and TIR images. To fully understand and leverage existing datasets and to allow for full transparency and repeatability, we provide comprehensive information and metadata, including complete documentation of the dataset and technical methods.

2 Site description

The study area is located in the Kunlun Mountain Pass (KMP) in the QTEC, where the QTH, QTR, and power/communication towers are crisscrossed (Luo et al., 2018a). They are densely situated across a width of 200 m, and a variety of projects occur on permafrost slopes connected by supporting bridges or laying towers or directly on roadbeds. The KMP is located in the hinterland of the QTP and in the middle of the East Kunlun Mountains, adjacent to the giant main fault in the northern part of the plateau, which controls its formation and development (Wu et al., 2017). In the KMP, thick early Quaternary sediments were deposited, and the sedimentary strata recorded the history of tectonic evolution in the northern part of the QTP. The MAAT in the KMP is -4°C , and the mean annual ground surface temperature (MAGST) ranges from -2.4°C to 3.2°C at a depth of approximately 15 m below the ground surface. The monthly air temperature ranges from a minimum of -28°C in winter to a maximum of 18°C in summer. The mean annual total precipitation ranges from 300 to 500 mm, and precipitation occurs most frequently from May to September, accounting for 80% of the annual total precipitation, with the highest precipitation occurring from July to August. Permafrost is well developed with a high ice content, and the active layer thickness (ALT) is more than 3 m, which is generally present above 4200 m in the region. Permafrost can be found in mountains and basins, but most of the valleys do not contain permafrost. ~~Moreover~~Through drilling data near the study area, the permafrost thickness ranges from 46 to 112 m, the temperature gradient within the frozen soil is $3.45^{\circ}\text{C}/100\text{ m}$, and the geothermal gradient below the frozen soil is $3.9^{\circ}\text{C}/100\text{ m}$ ~~(Luo et al., 2019)~~(Luo et al., 2019; Yang et al., 2017).

Two slopes (slopes A and B) within the KMP were selected (Figure 1). Slope A ($94^{\circ}03'46''\text{ E}$, $35^{\circ}39'4''\text{ N}$, 4759 m a.s.l.) is located along the side of the QTH, while the QTR, supported by bridges, runs across slope B ($94^{\circ}03'48''\text{ E}$, $35^{\circ}38'45''\text{ N}$, 4770 m a.s.l.), and the QTH is next to slope B. A large number of similar permafrost slopes have been found along the QTEC, but few projects are densely distributed on permafrost slopes. Therefore, the study area is considered to be an excellent place for observing the interaction of hydrological-thermal deformation effects between engineering operations and permafrost slopes.

~~Through drilling data, the~~The active layer is mainly composed of clay from the top of the soil to a depth of 270 cm, including wet silty clay from 0 to 50 cm, loose silty clay from 50 to 120 cm, compacted clay from 120 to 180 cm, saturated clay mud from 180 to 230 cm, loose silty clay with gravel from 230 to 250 cm, and thick underground ice from 250 to 270 cm. According to the soil profile, the types of permafrost on the above two slopes can be classified as ice-rich permafrost, ~~and the ATL here is generally larger than 3 m.~~ The vegetation type in this area is a typical alpine desert steppe. The vegetation on slope A is sparse, at a coverage lower than 5%, and most of the vegetation is gathered at the top of the slope, while slope B contains almost no vegetation.

From 2014-2017, four deformation monitoring campaigns using TLS with GNSS and soil hydrothermal in situ monitoring were deployed. Moreover, a UAV system equipped with RGB and TIR sensors was adopted to monitor the spatiotemporal changes in the ecological environment and ground surface temperature of the slopes. The deployment of these instruments provides an integrated dataset for hydrological-thermal deformation monitoring of permafrost slopes and the various frozen soil projects (QTR, QTH, and power/communication towers) located on (middle) or near them.

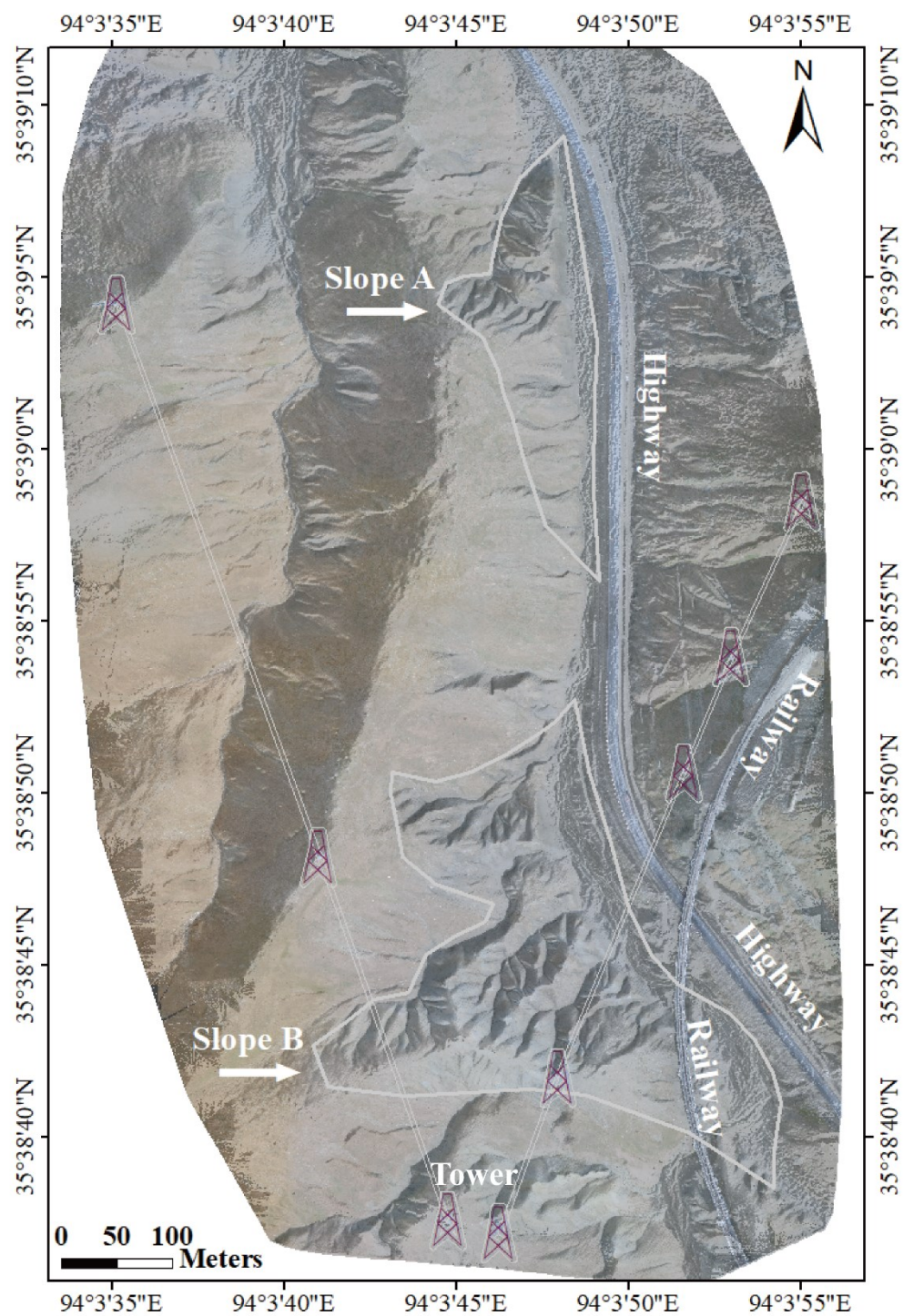


Figure 1. Geography of the study area, including the two permafrost slopes A and B, Qinghai-Tibet Highway and Railway, and power/communication towers.

3 Data description

3.1 Meteorological observations

140 Observation of meteorological factors was conducted at two permanent meteorological stations (Golmud and Wudaoliang) and one field meteorological station (Xidatan) ~~with daily meteorological records for the period from 2014 to 2018~~ (Table 1), which were retrieved from the National Meteorological Information Center (NMIC, <http://data.cma.cn>). The two weather stations are located on the north and south sides of the two slopes and are also the closest national weather stations to the two slopes. The meteorological database includes the daily mean, maximum (max), and minimum (min) air temperatures, wind speed, observed and corrected precipitation, evaporation, air humidity, atmospheric pressure, sunshine duration, daily mean, max, and min ground surface temperatures, and the soil temperature at different depths (i.e., 5, 10, 15, 20, 40, 50, 80, 160, and 320 cm). Golmud and Wudaoliang are two national reference meteorological stations in China, while Xidatan is a national general field station. Although these two national meteorological stations are far from the above two slopes, the data obtained from these meteorological stations are very valuable in this harsh environment. Their data can be combined with the data obtained from the Xidatan field station to analyze the spatiotemporal dynamics of the permafrost slopes in the corridor.

150 Meteorological station Golmud (94°54' E, 36°25' N, 2808 m a.s.l.) is located in the urban area of Golmud, south of the two slopes, with few surrounding buildings. This weather station area is located in the seasonal frozen soil zone. The distance between the station and the two slopes is approximately 115 km.

The meteorological station Xidatan (94°08' E, 35°43' N, 4538 m a.s.l.) is located in the northern part of the two slopes and is the closest field weather station to the two slopes. The distance between the station and the two slopes is approximately 9.7 km. The Xidatan field station is 300 m away from the QTH and is located at the northernmost end of the permafrost in the QTEC. The vegetation type on the underlying surface is an alpine meadow. Figure 2 shows the data for this station. Observation data were retrieved from the National Tibetan Plateau Data Center (NTPDC, <https://data.tpdac.ac.cn/>).

160 The meteorological station Wudaoliang (93°05' E, 35°13' N, 4612 m a.s.l.) is located to the north of the two slopes in a continuous permafrost zone, next to the 109 National Highway along the QTH. The distance between the station and the two slopes is approximately 101 km.

Table 1. List of meteorological observation data, where n/a indicates not applicable. Automated observations were conducted at the Golmud and Wudaoliang stations in 2000 and 2001, respectively.

SID	Station name	Longitude	Latitude	Elevation	Automatic	From year	To year	Source
					station model			
52818	Golmud	94°54'	36°25'	2808	Vaisala Milos 500	1955	2018 2020	NMIC

XTDMS	Xidatan	94°08′	35°43′	4538	n/a	2014	2018	NTPDC
52908	Wudaoliang	93°05′	35°13′	4612	Vaisala Milos 500	1956	2018 2020	NMIC

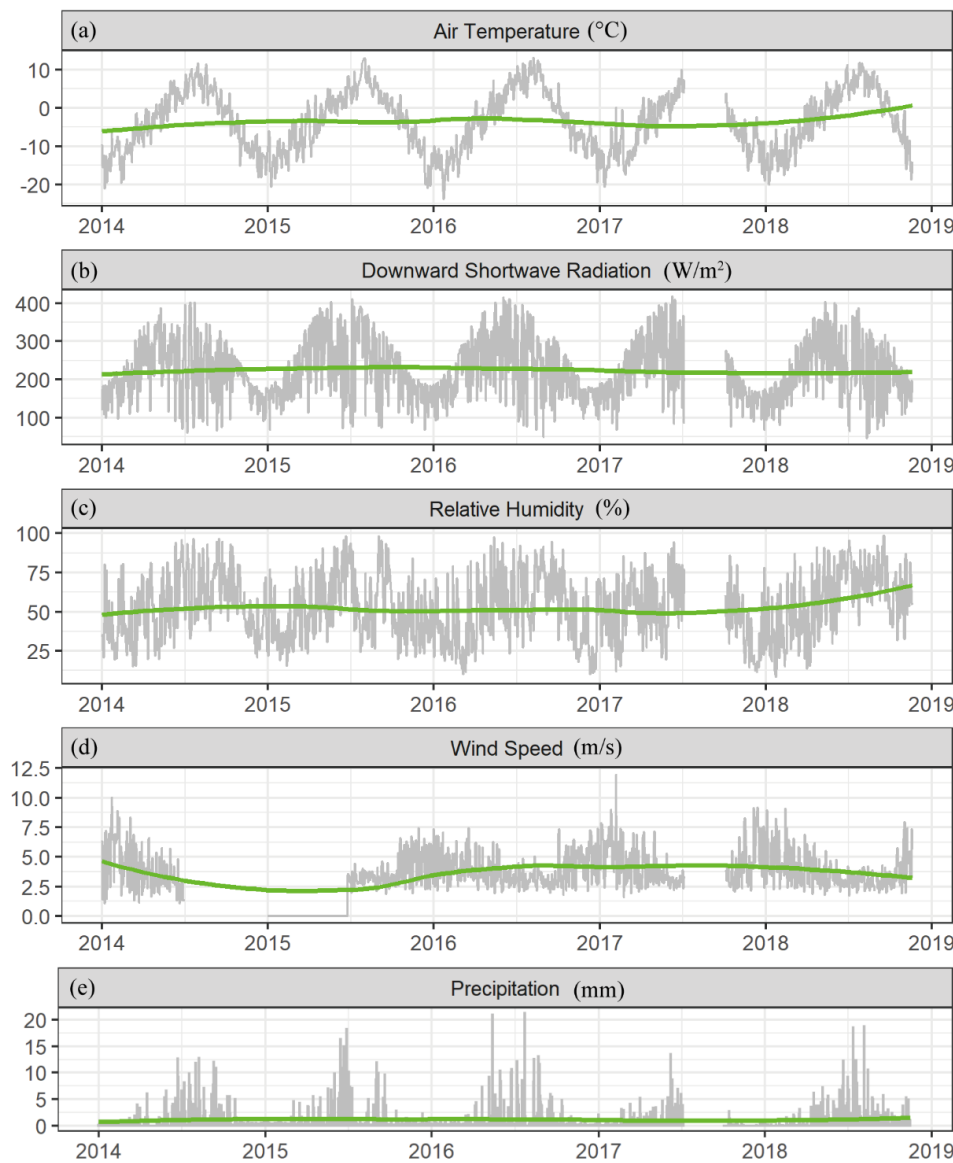


Figure 2. Time series (daily mean values) of the Xidatan field station from 2014 to 2018: (a-e) meteorological observation data.

Changes in soil temperature and humidity can be used to indicate water and heat transfer processes, which will strongly affect the physical and mechanical properties of frozen soil and will further affect the stability of slopes. The ground temperature and moisture data from the near-surface to within 270 cm in the study area were recorded. In situ ground observations were deployed starting in July 2013 in the active layer of slope A at 11 depths (1, 30, 63, 80, 100, 123, 140, 175, 205, 235, and 260 cm), using thermocouple probes (105T, Campbell Scientific) to measure the soil temperature and using 11 time-domain reflectometer (TDR) probes (model CS615-L, Campbell Scientific) at 11 depths (10, 20, 48, 74, 91, 110, 135, 157, 190, 220, 245, and 270 cm) to measure the soil volumetric water content from 2014 to 2018 (Figure 3). The TDR probes were mounted horizontally along the soil profile next to the temperature probes at the different soil depths, and measurements were recorded once per hour. Since the soil undergoes a freezing period from refilling to compaction, the 2013 data are not analyzed. A Campbell Scientific CR1000 data logger is used to connect the ground temperature and volumetric water content probes. Figure 4 shows the kriging interpolation data of the soil temperature and volumetric water content at the different depths from 2014 to 2019 in the study area. ~~All three~~ The two permanent meteorological stations also contain ground observation data. Soil moisture with a soil temperature below 0 °C is beyond the scope of instrument monitoring. Monitoring soil moisture under frozen conditions has always been a technical difficulty. Therefore, soil moisture data below 0 °C are not available.



Figure 3. Ground sensor installation.

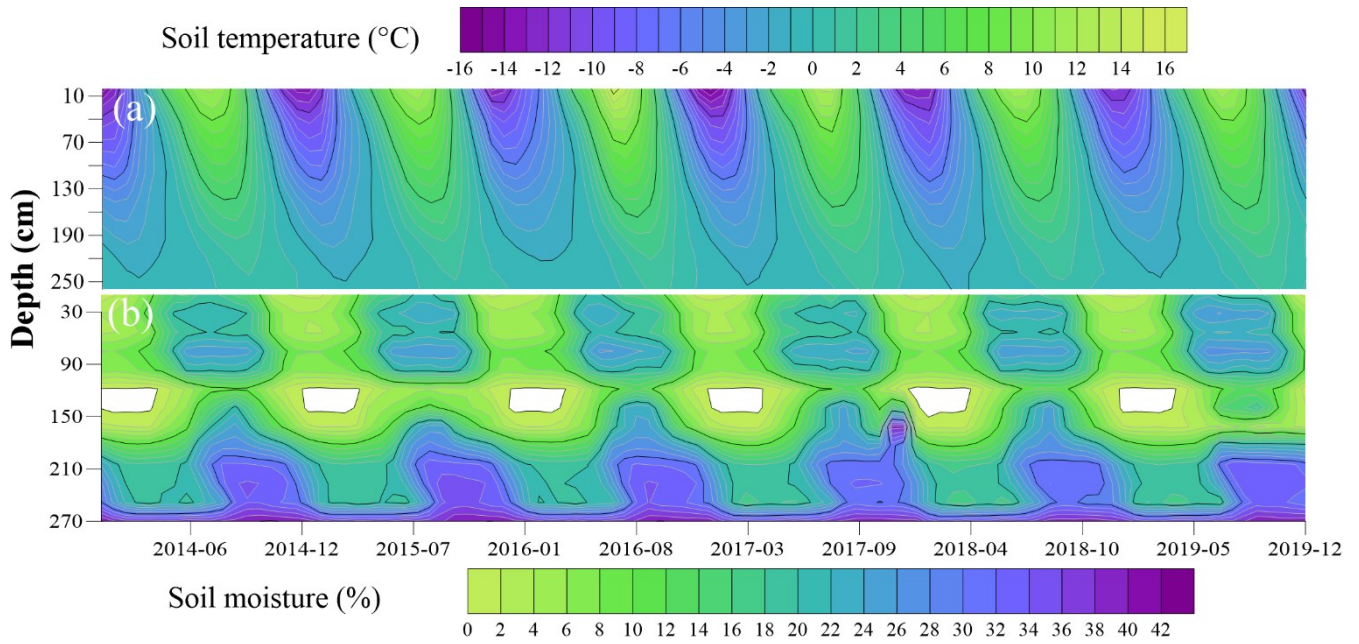


Figure 4. Soil temperature and volumetric water content from 2014 to 2019. (a) Soil temperature (°C); (b) soil moisture (%).

3.3 TLS and GNSS

Deformation monitoring was performed through TLS with a network real-time kinematic (RTK) service provided by the National Geodetic Control Network (NGCN) for the China Geodetic Coordinate System 2000 (CGCS 2000) at permanent reference stations for the GNSS (Figure 5a and 5b). A FARO Focus^{3D} X130 3D laser scanner and six Trimble 5700 GNSS systems were deployed at the study site between May 2014 and October 2015. Two GNSSs were adopted as datum points 30 km outside the study area (Figure 5c and 5d), and another four GNSSs were deployed as reference points around one of the slopes. According to the manufacturer's specifications, the FARO TLS instrument measures 3D coordinates with a distance accuracy up to ± 1 mm, and the ranging error is ± 2 mm. The Trimble 5700 GNSS systems achieve a measurement accuracy of ± 5 mm + 0.5 ppm root mean square (RMS) horizontally and ± 5 mm + 1 ppm RMS vertically for static and FastStatic GPS surveying, respectively.

Since May and October are the transition periods of the freeze-thaw cycle, we conducted monitoring campaigns in the months of May and October between May 2014 and October 2015. The successive three freeze-thaw phases are referred to as the first thaw (May 2, 2014 to October 10, 2014), first freeze (October 10, 2014 to May 3, 2015), and second thaw (May 3, 2015 to October 4, 2015). The above two slopes mainly manifested melting collapse during thawing and frost heave during freezing, but after several freeze-thaw cycles, frost heave dominated (Figures 6 and 7). A full slope scan requires approximately 30 scan positions to generate 3D point cloud data. Each scan requires the placement of six white reference spheres at the study site, and they are visible at all scan locations. Two to three of these reference spheres are moved for the next scan. Six reference sphere data points can be combined with the GNSS data to georeference, register, align, and mosaic the point cloud data of the

TLS instrument with FARO SCENE and Geomagic Studio software. TLS monitoring data show that during the thawing period, the slopes were dominated by subsidence, while during the freezing period, the slopes were dominated by frost heave. After multiple thawing cycles and one freezing cycle, the slopes also exhibit frost heave characteristics (Luo et al., 2019).

As a supplement to the TLS point cloud data, we prepared Sentinel-1 deformation data ~~for~~during the freeze-thaw ~~stage~~stages in the study area from 2014 to 2020 using interferometric synthetic aperture radar (InSAR) technology.

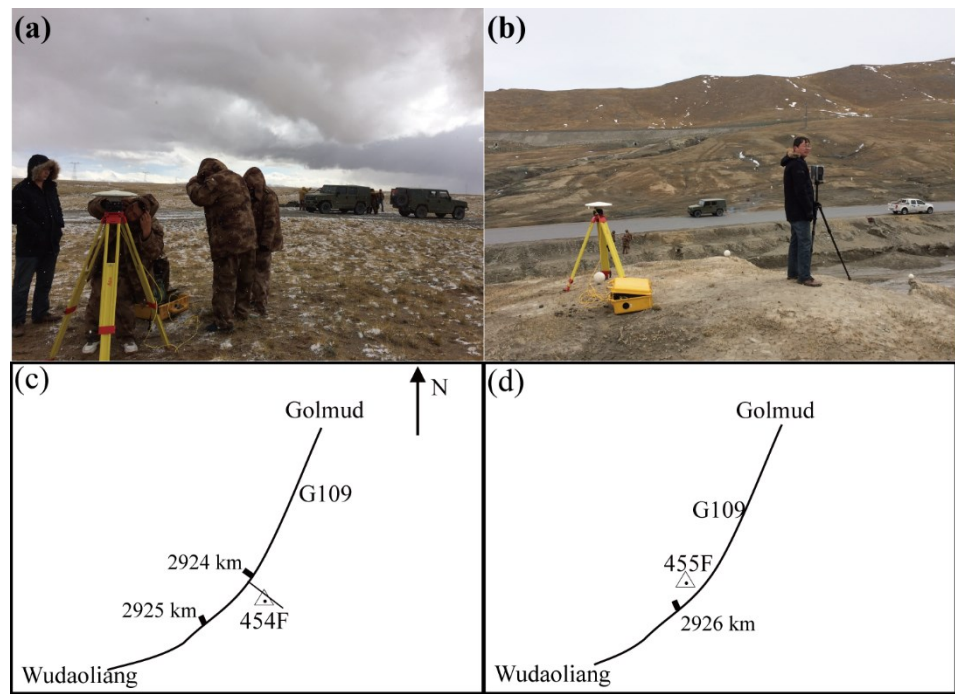


Figure 5. TLS observation with the GNSS from 2014 to 2015. (a) Datum station of the GNSS; (b) TLS observation with the GNSS and white reference sphere set; (c) datum station 454F; (d) datum station 455F.

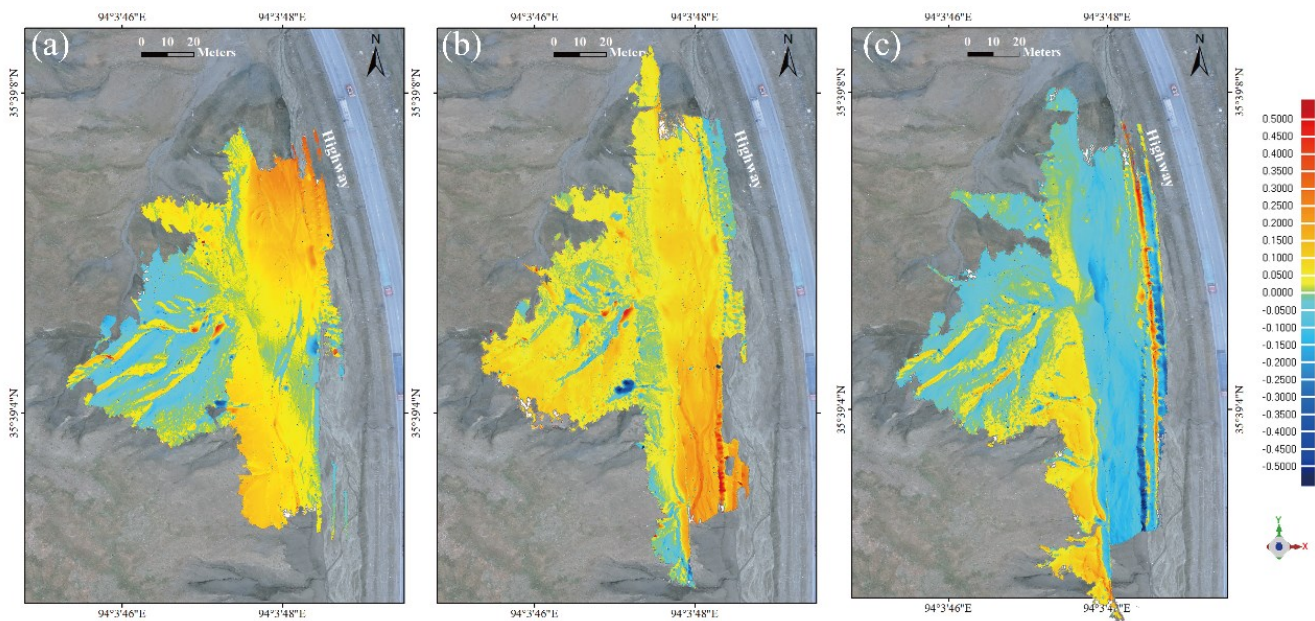


Figure 6. Deformation of slope A during the first thaw, first freeze, and second thaw. (a) First thaw; (b) first freeze; (c) second thaw.

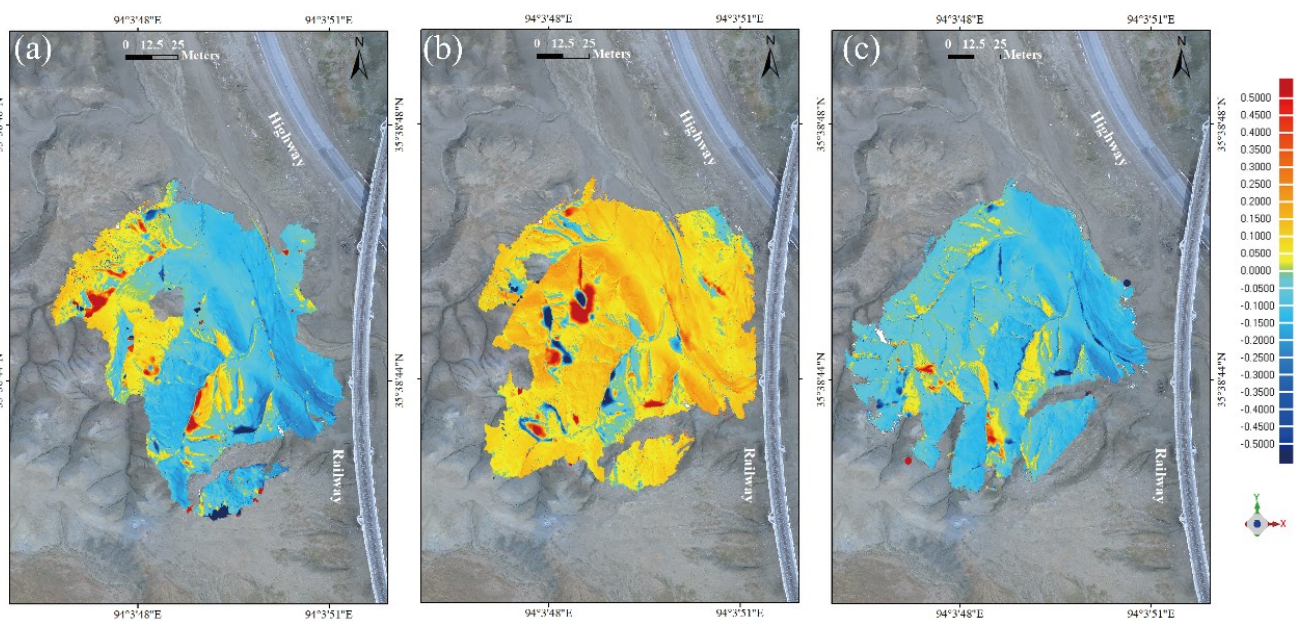


Figure 7. Deformation of slope B during the first thaw, first freeze, and second thaw. (a) First thaw; (b) first freeze; (c) second thaw.

The change in frozen soil is greatly affected by the temperature. To monitor the heat exchange between the two slopes and the engineering infrastructure around them, a UAV system with mounted RGB and TIR sensors was adopted (Luo et al., 2018a). The DJI Inspire 1 UAV system (DJI, Inc., Shenzhen, China) weighs approximately 2.85 kg, including propellers and batteries, and is equipped with a Zenmuse X3 RGB camera and a Zenmuse XT TIR sensor. The camera and sensor weigh 221 g and 270 g, respectively. The UAV is also equipped with GPS and an inertial measurement unit (IMU) to measure the geographical and flight positions, respectively. The TIR sensor has a resolution of 336×256 pixels, a thermal sensitivity of < 0.05 °C at f/1.0, a field of view of 17° (H) \times 13° (V), a focal length of 19 mm, and a spectral response in the electromagnetic spectrum. The above TIR sensor has a range from 7.5 to 13.5 μm . A mobile phone equipped with a flight control system app is used to control the flight of the UAV, in addition to DJI GO and Pix4D capture software. ~~Regardless of the RGB or TIR sensor, the JPG data format is selected.~~ Both instruments adopt vertical angles to capture images, with RGB overlap rates above 75% and TIR overlap rates above 80%.

Figure 8 shows the drone flight over the slopes. The two permafrost slopes were subjected to four flight experiments with UAV-mounted RGB and TIR sensors in 2016 and 2017. The TIR flight experiments lasted from morning to afternoon, with intervals of 1 to 2 hours (Table 2). The RGB datasets were processed with pix4dmapper software to generate digital surface model (DSM) and orthorectification images. ~~The TIR data formats selected for 2016 and 2017 were TIF and JPG, respectively.~~ The TIR images were processed with the software program FLIR Tools (FLIR System Inc., USA) (Figure 9), and ground surface temperature differences were analyzed to determine the effects of the different permafrost engineering operations on the slopes (Figure 10). This study analyzes the thermal impact of engineering operations on permafrost slopes. The projects and the slope were divided according to a width of 2 m, and then the surface temperature of the project and the temperature between different zones of the surrounding slope were compared. When these temperature differences appear at the first break point, this is the largest thermal impact of the project on the slope. The distance between the slope zone and the project is the maximum range of thermal influence (Luo et al., 2018a). The results show that the QTH has the greatest thermal impact on permafrost slopes, followed by the QTR and finally the power/communication towers.

Table 2. UAV flight time from 2016 to 2017.

Flight Date yyyymmdd	Flight Time hh:mm	Height m	Slope	Sensor
20160417	13:36-13:56	20-120	Slopes A and B	RGB
20160830	10:18-13:55	120	Slopes A and B	RGB
20170822	11:26-13:46	120	Slopes A and B	RGB
20160830	12:47-12:52	30	Slope A	TIR
20170722	11:00-15:51	150	Slopes A and B	TIR
20170823	10:30-17:25	150	Slopes A and B	TIR

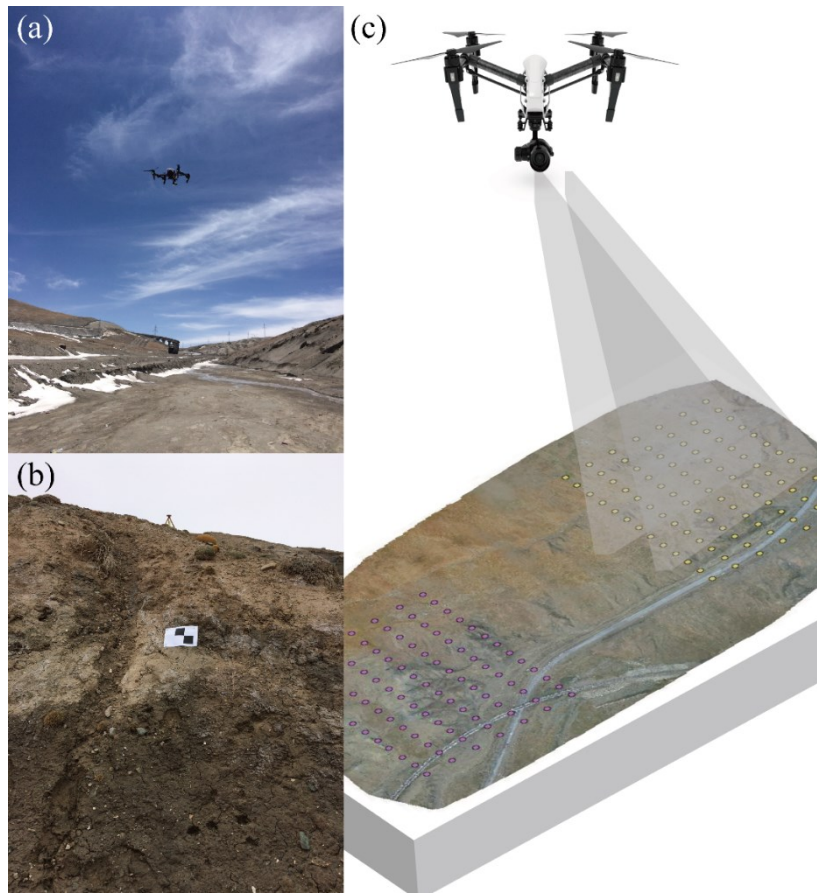


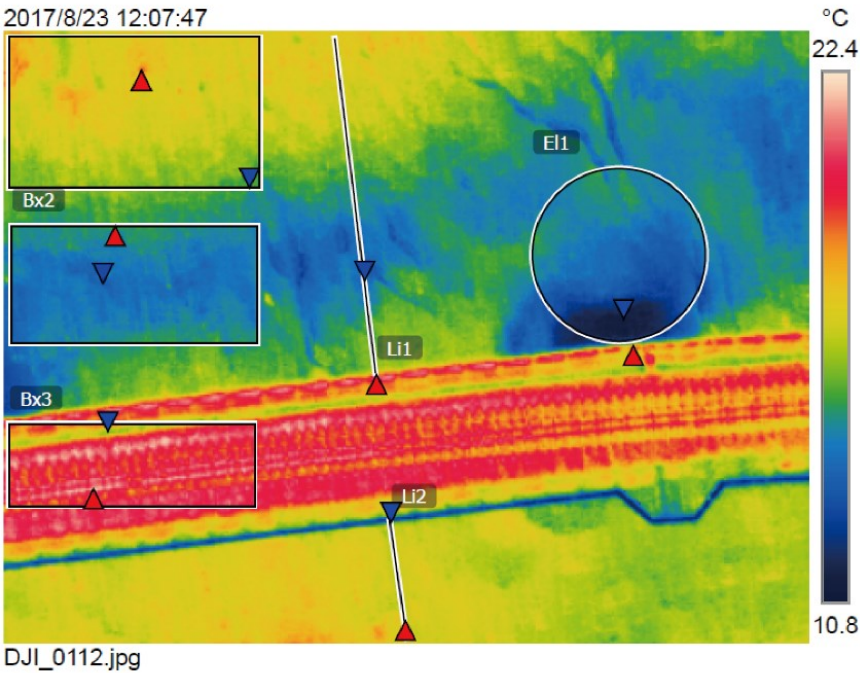
Figure 8. UAV field observations from 2016 to 2017. (a) UAV under observation; (b) GNSS and rectangular white–black cardboards; (c) UAV flight path over the two permafrost slopes.

Measurements

Bx1	Max	19.2 °C
	Min	15.0 °C
	Average	17.1 °C
Bx2	Max	16.0 °C
	Min	13.3 °C
	Average	14.5 °C
Bx3	Max	22.4 °C
	Min	15.9 °C
	Average	19.9 °C
El1	Max	18.1 °C
	Min	10.8 °C
	Average	13.7 °C
Li1	Max	18.8 °C
	Min	13.6 °C
	Average	15.6 °C
Li2	Max	17.4 °C
	Min	15.0 °C
	Average	16.9 °C

Parameters

Emissivity	1
Refl. temp.	22 °C



255

Figure 9. Analysis of the ground surface temperature using UAVs with TIR sensors, and the Qinghai-Tibet Railway as an example.

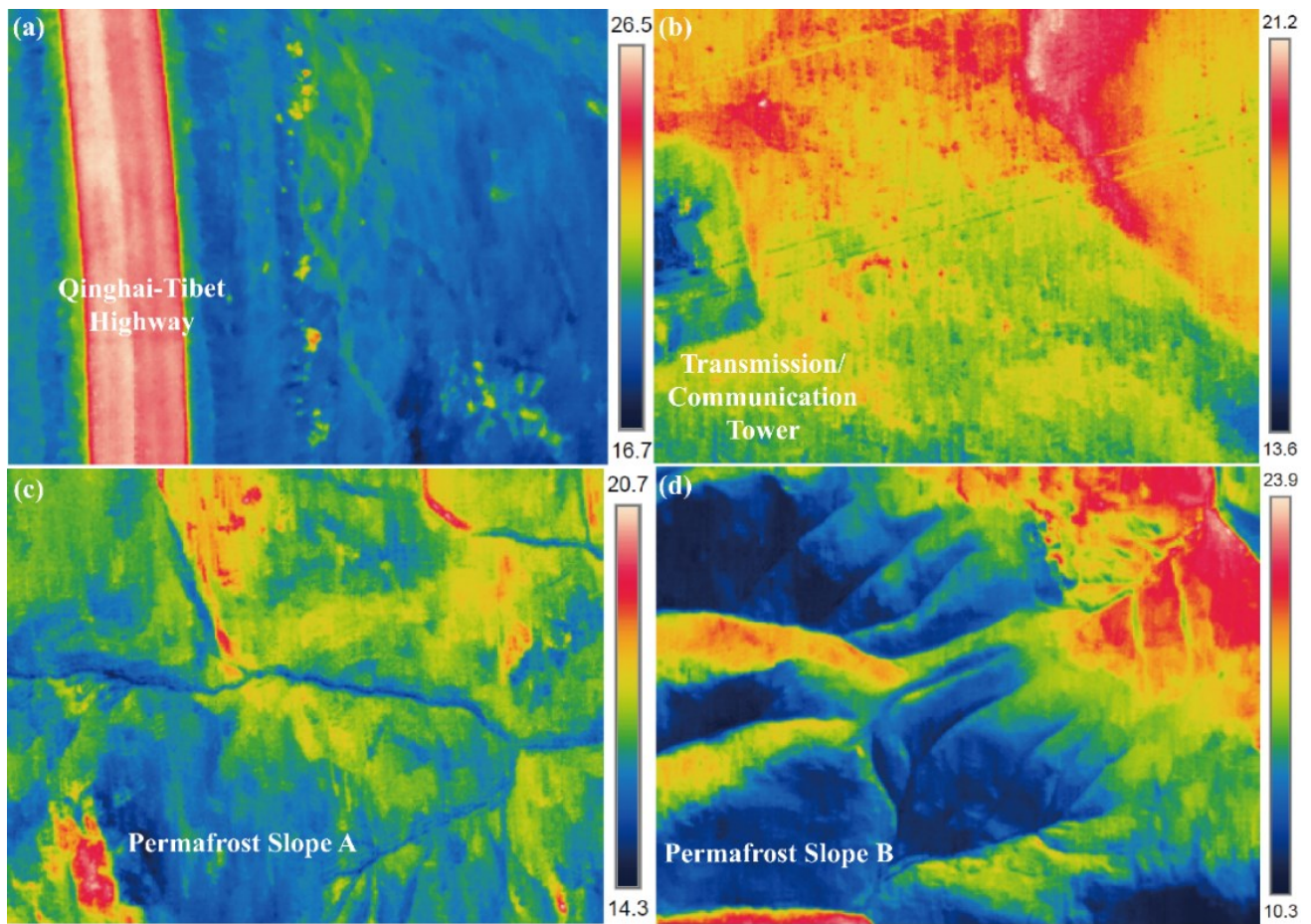


Figure 10. Ground surface temperature using UAVs with TIR sensors. (a); Qinghai-Tibet Highway; (b) power/communication tower; (c) slope A; (d) slope B.

4 Data quality control

The meteorological data have undergone quality control. First, all suspicious and incorrect data were manually re-examined and corrected. For example, a new column of “Corrected_P” has been added to the precipitation data based on the original data, and this column of data is the result of the manual revision. Ultimately, all feature data are marked with a quality control code (Table 3). In terms of the instantaneous meteorological values, if data are missing due to collector or communication issues, the terminal directly generates missing data when the terminal commands the data input, and the corresponding quality control identifier is 8. If there are no missing data, the quality control is assessed to be incorrect at the terminal. When the command data are output, values are still generated, and the corresponding quality control identifier is 2, but the erroneous data do not participate in the subsequent related calculations or statistics.

After quality control, the availability of the various weather elements is usually higher than 99%, and the correct data transmission rate approaches 100%.

The use of GNSS and white reference spheres can improve the accuracy of TLS monitoring, while the use of GNSS and rectangular white–black cardboards can improve the accuracy of UAV monitoring (Luo et al., 2019). By measuring the ground reference and control points of the TLS, the GNSS is used to ensure the orientation and registration of the different 3D datasets in the common coordinate system. The spherical shape achieves the maximum scanning efficiency in all directions and has proven to be the most effective laser scanning target, which can be used in conjunction with the GNSS datum points (454F and 455F) and control points to register, align, and mosaic the TLS data. These GNSS instruments collect data on the ground reference points to ensure the maximum geospatial accuracy, and they are subject to stringent ground controls to reference and calibrate the 3D FARO laser scanner. Moreover, the 3D laser scanner and GNSS obtain continuous, high-precision spatial deformation data on the slopes, and we can compare the spatial changes over time through the GNSS network. These targets are used for registration and as georeferences and checkpoints. Therefore, their positioning accuracy directly affects the accuracy of the data processing results. Data preprocessing is proposed to determine the scope of the slope, filter any noise points, and repair data gaps. Semiautomatic and manual processing is conducted to filter the noise points and repair the gaps in the point cloud datasets (Luo et al., 2019). Due to the high moisture content in the lower part of the slope, monitoring is easily disturbed by vibrations, resulting in noise. At the top of slope A, large wild animals such as wild donkeys were observed. Therefore, the deformation of the slope is also affected by the trampling of wild animals and should be taken into account in the analysis.

Table 3. Quality control codes for the meteorological station data. The variable names are suffixed with _QC.

Quality control code	Description
0	Correct data, no modification
1	Suspicious data, no modification
2	Error data, no modification
3	Missing data, no modification
4	Data with revised values
5	Originally suspicious data, has been modified
6	Originally error data, has been modified
8	Originally missing data, has been modified
9	No data quality control

5 Data and code availability

All data and R code presented in this paper are available from Zenodo (<https://zenodo.org/communities/qtec>; last access for all Zenodo links: ~~29 April 2019~~ 2 June 2021), which provides a dataset view and download statistics. The data and code with open access (including links to the subsets) can be found on either repository via the following links:

- Meteorological and ground observations:
<http://doi.org/10.5281/zenodo.4588099> ~~4588099~~ 4879639 (Luo et al., 2020d)
- TLS measurements:
<http://doi.org/10.5281/zenodo.4588090> (Luo et al., 2020a)
- UAV RGB and TIR images:
<http://doi.org/10.5281/zenodo.4686506> ~~4686506~~ 4879850 (Luo et al., 2020b)
- R code of permafrost indices and visualization:
<http://doi.org/10.5281/zenodo.4686141> (Luo et al., 2020c)

6 Summary and outlook

Slope failure in permafrost regions, caused by permafrost degradation and ground ice melting, affects the engineering infrastructure and permafrost environment in the Qinghai-Tibetan Engineering Corridor. Most of the current studies are based on the interaction between individual engineering projects and permafrost slopes by means of multipoint monitoring, interpolation, or simulation, but the dense layout of the various projects and the fragile and sensitive permafrost slopes in the corridor have rarely been previously studied as a whole. The permafrost slopes and various projects (QTR, QTH, and power/communication towers) located in the corridor are chosen as the research objects, and 3D terrain change monitoring technology using TLS and GNSS, low-altitude remote sensing technology using drone-based visible and TIR, and in situ monitoring technology was deployed, combined with image mosaic, three-dimensional modeling, and spatial analysis. This dataset contains both site and space features on both the surface and underground horizons, including the ground hydrothermal state, spatial ground surface temperature, slope deformation and meteorological data, thus establishing a comprehensive monitoring dataset for the QTP permafrost slopes and surroundings (QTR, QTH, etc.). The dataset will be of great value to examine the hydrological-thermal deformation of permafrost slopes under the influence of climate change and engineering disturbances, as well as to reveal the mutual feedback between the slopes and engineering infrastructure, evaluate the potential hazards of long-term stability and safety operation of the engineering infrastructure and slopes, and provide data support for the safety range and layout of the proposed permafrost engineering infrastructure.

Appendix A: Symbols and Abbreviations

	CGCS	China Geodetic Coordinate System
	DSM	Digital surface model
	GNSS	Global navigation satellite system
325	InSAR	Interferometric Synthetic Aperture Radar
	KMP	Kunlun Mountain Pass
	MAAT	Mean annual air temperature
	MAGST	Mean annual ground surface temperature
	MAGT	Mean annual ground temperature
330	NGCN	National Geodetic Control Network
	NMIC	National Meteorological Information Center
	QTEC	Qinghai-Tibet Engineering Corridor
	QTH	Qinghai-Tibet Highway
	QTP	Qinghai-Tibet Plateau
335	QTR	Qinghai-Tibet Railway
	RTK	Real-time kinematic
	TDR	Time-domain reflectometry
	TIR	Thermal infrared
	<u>TLS</u>	<u>Terrestrial laser scanning</u>
340	TTOP	Temperature at the top of the permafrost
	TLS	Terrestrial laser scanning
	UAV	Unmanned aerial vehicle

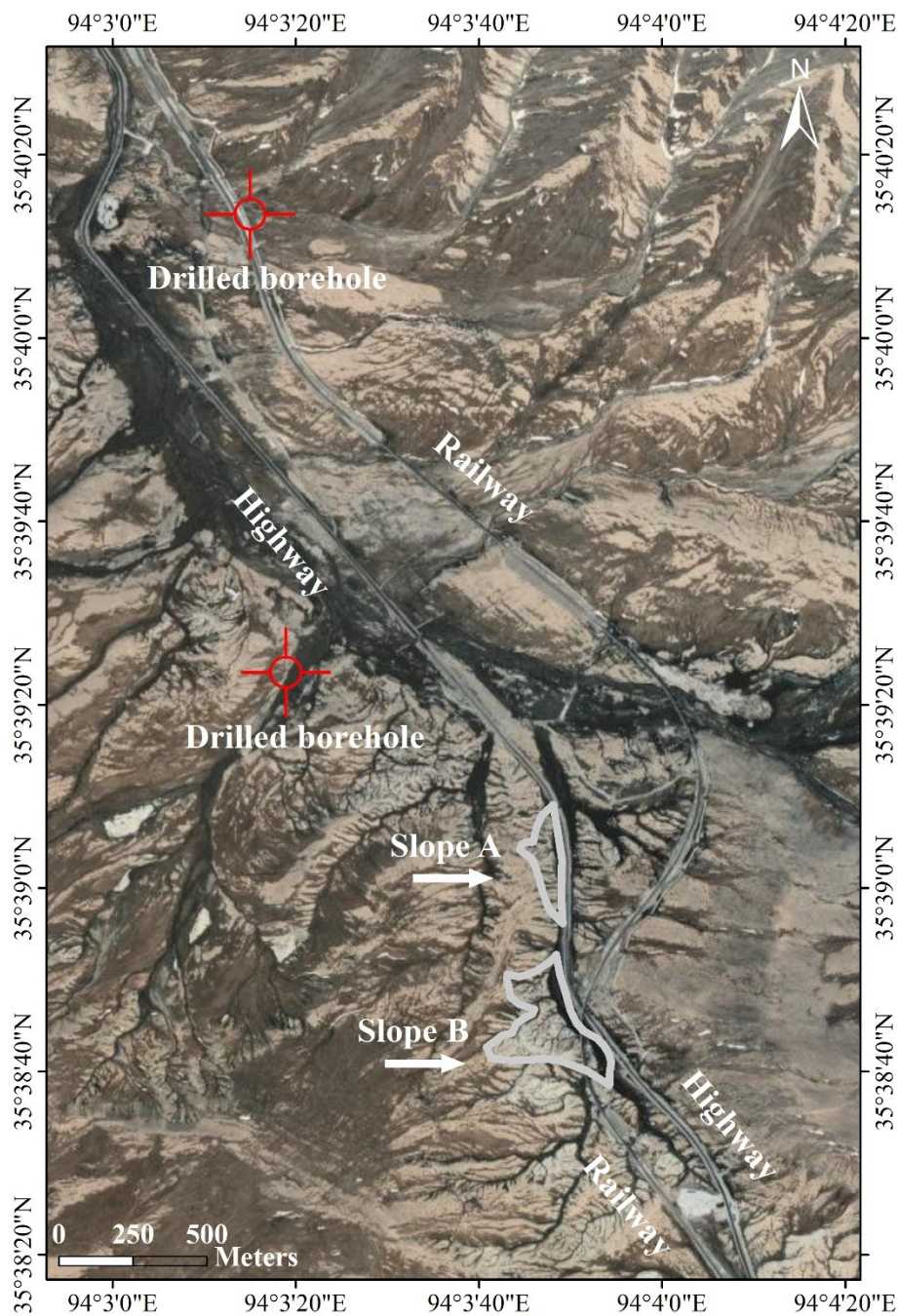


Figure B1: The location of two drilled boreholes.

Appendix C: Classification of frozen soil

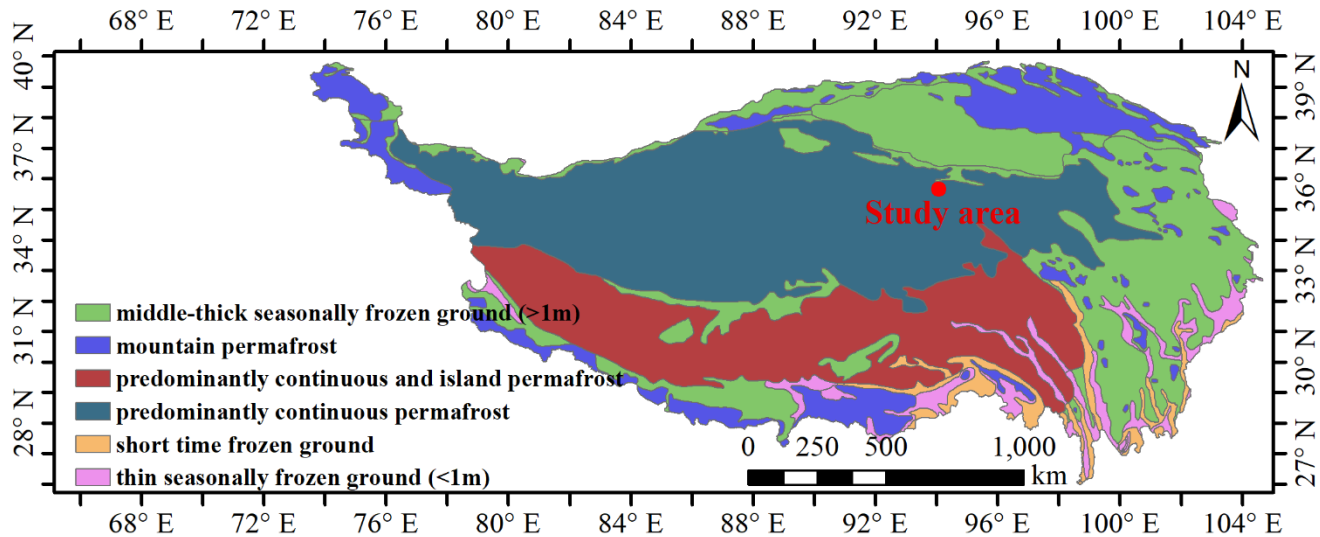


Figure C1: The frozen soil distribution in the study area.

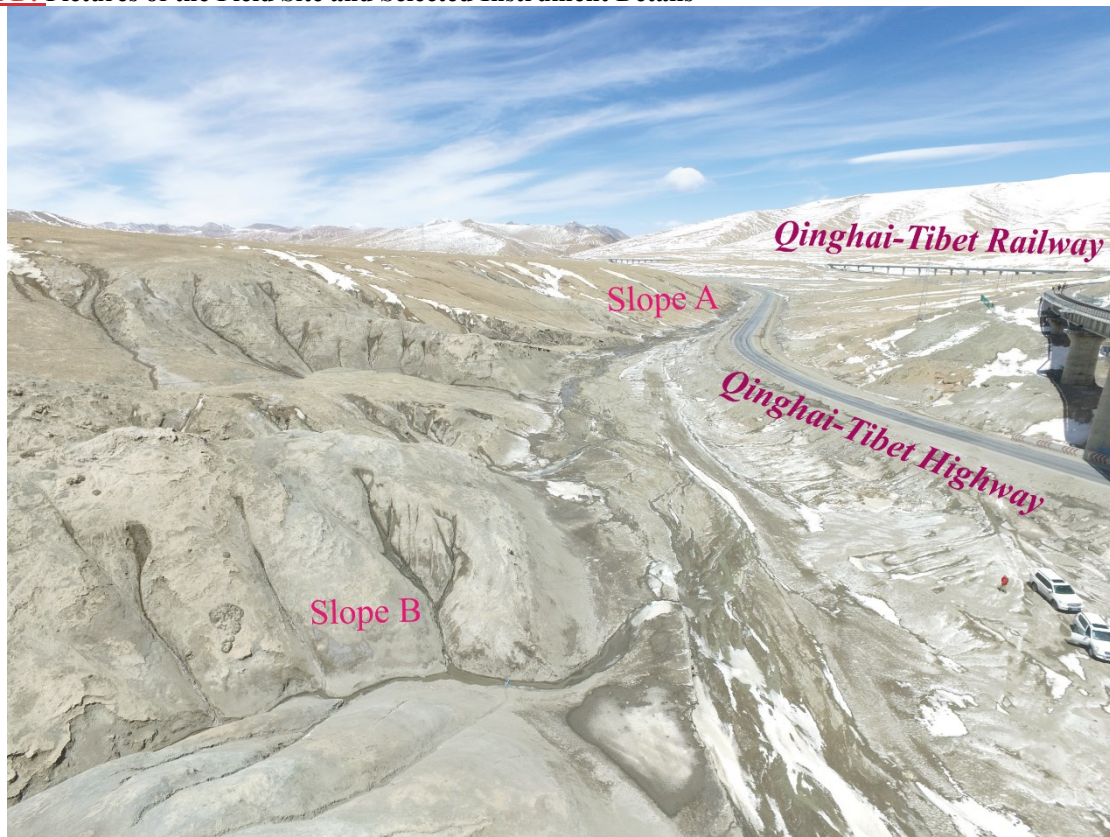


Figure B4D1. Slopes A and B, with the QTH and QTR clearly visible.



360 **Figure B2D2.** Slope B. The railways and power/communication towers are clearly visible.

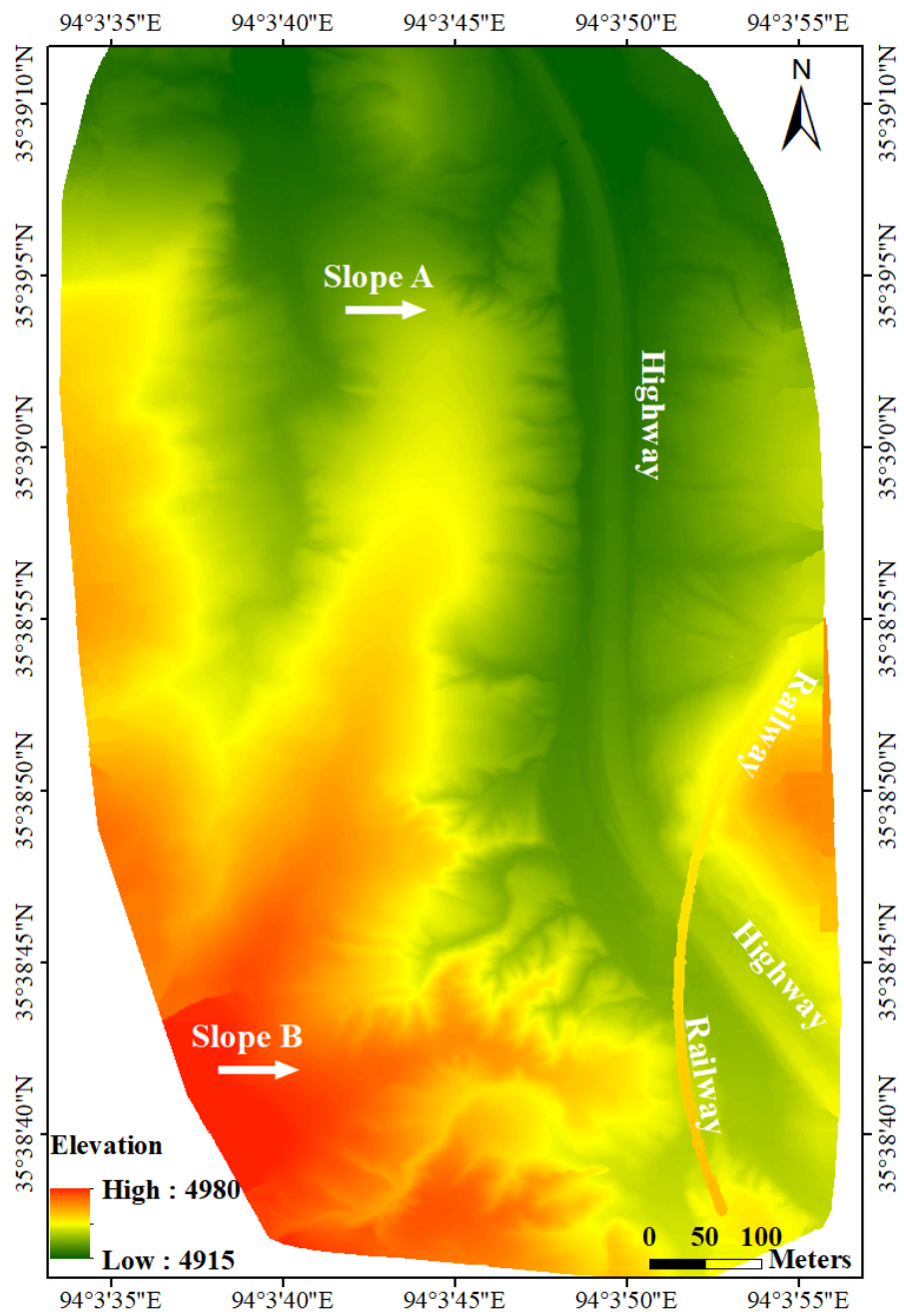


Figure **CE1**. DSM by the UAV. (a) Slope A; (b) slope B.

365

Appendix DE: Names of the Variables and Units for the Data Files

375 **Table D4F1.** Overview of the meteorological and ground observation data. The suffixes _MIN, _MAX, _AVG, and _QC indicate the minimum, maximum, ~~and~~ average values, and quality control code of the variable, respectively, while 32766, NA, and NAN indicate null values. The suffix of TotalPrecip with “20_8”, “8_20”, and “20_20” are the total precipitation from 20 to 8 o'clock the next day, 8 to 20 o'clock, and 20 to 20 o'clock the next day, respectively. The suffixes of Evaporation with “SmallEvaporators” and “LargeEvaporators” are the data monitored by the small and large evaporator respectively. The suffix of GT with a number indicates the ground temperature in centimeters.

380

Variable Name	Description	Unit	Scale
Temperature	Air temperature	°C	0.1
Tmax	Maximum air temperature	°C	0.1
Tmin	Minimum air temperature	°C	0.1
Wind	Wind speed	m/s	0.1
Precip	Precipitation	mm	0.1
Corrected_P	Corrected precipitation	mm	0.1
Evaporation	Evaporation	mm	-
Humidity	Air humidity	%	-
Press	Atmospheric pressure	hPa	0.1
Sunshine	Sunshine duration	h	0.1
GT	Ground temperature	°C	0.1

Variable Name	Description	Unit
Temperature	Air temperature	°C
Wind	Wind speed	m/s
WindDirection	Wind direction	16 direction
Extreme_Wind	Extreme wind speed	m/s

<u>WindDirection_Extreme_Wind</u>	<u>Wind</u> <u>direction</u> <u>with</u> <u>extreme</u> <u>wind speed</u>	<u>16</u> <u>direction</u> <u>s</u>
<u>TotalPrecip</u>	<u>Precipitatio</u> <u>n</u>	<u>mm</u>
<u>Corrected_P</u>	<u>Corrected</u> <u>precipitatio</u> <u>n</u>	<u>mm</u>
<u>Evaporation</u>	<u>Evaporatio</u> <u>n</u>	<u>mm</u>
<u>Humidity</u>	<u>Air</u> <u>humidity</u>	<u>%</u>
<u>Press</u>	<u>Atmospher</u> <u>ic pressure</u>	<u>hPa</u>
<u>Sunshine</u>	<u>Sunshine</u> <u>duration</u>	<u>h</u>
<u>GT</u>	<u>Ground</u> <u>temperatur</u> <u>e</u>	<u>°C</u>

带精

Appendix EG: Physical Parameters of Engineering Infrastructure

Table EG1. Physical parameters of the engineering infrastructure near the permafrost slopes. Two types of foundations are applied in the construction of the power/communication towers, i.e., * the cone-cylinder spread footing and # the drilled shaft.

Engineering	Variable	Value
Highway	Subgrade height	2.0-2.5 m
	Road width	9 -10 m
	Track width	6.5 m
Railway	Bridge diameter	4.5 m
	Bridge height	-16.5 m
	Buried base depth	3.7-5.8 m
Tower	Base width of foundation*	3.5-6.4 m
	Diameter of piles#	~ 1.0 m
	Length of piles	7.0 -16.0 m

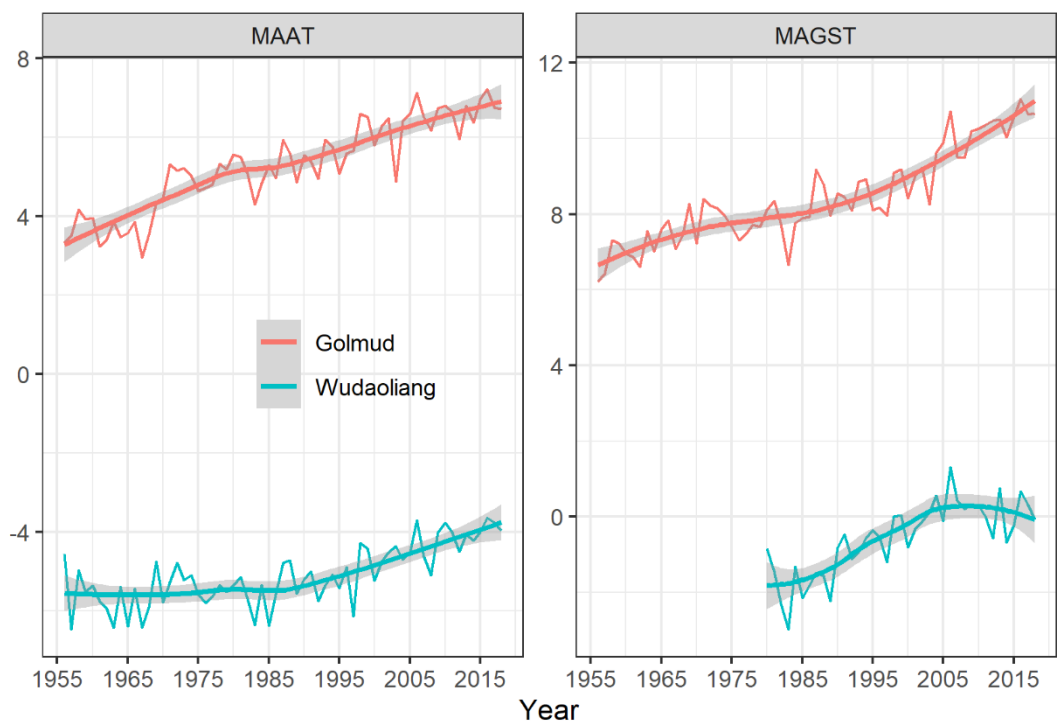


Figure F4H1. Mean annual air temperature (MAAT, °C) and mean annual ground surface temperature (MAGST, °C) at the meteorological stations Golmud and Wudaoliang.

Author contributions. Lihui Luo, Yanli Zhuang, Yanmei Shi, and Li Wang initiated and set up the ground observational, TLS, GNSS, and UAV field experiments. Lihui Luo, Yanli Zhuang, and Zhongqiong Zhang compiled the database, performed the analysis, generated the figures, and wrote the paper. All authors contributed to the database compilation and assisted in writing the paper.

Competing interests. The authors declare that they have no conflicts of interest.

Acknowledgments. This research was jointly supported by the National Natural Science Foundation of China (41871065), the National Science Fund for Distinguished Young Scholars (41825015), the Key Research Project of Frontier Science of Chinese Academy of Sciences (QYZDJ-SSW-DQC040), and the Strategic Priority Research Program of the Chinese Academy of Sciences (XDA19090122).

References

Arenson, L. U., Kääb, A., and O'Sullivan, A.: Detection and Analysis of Ground Deformation in Permafrost Environments, Permafrost and Periglacial Processes, 27, 339-351, <https://doi.org/10.1002/ppp.1932>, 2016.

Bessette-Kirton, E. K., and Coe, J. A.: A 36-Year Record of Rock Avalanches in the Saint Elias Mountains of Alaska, With Implications for Future Hazards, Frontiers in Earth Science, 8, <https://doi.org/10.3389/feart.2020.00293>, 2020.

Boike, J., Nitzbon, J., Anders, K., Grigoriev, M., Bolshiyarov, D., Langer, M., Lange, S., Bornemann, N., Morgenstern, A., Schreiber, P., Wille, C., Chadburn, S., Gouttevin, I., Burke, E., and Kutzbach, L.: A 16-year record (2002–2017) of permafrost, active-layer, and meteorological conditions at the Samoylov Island Arctic permafrost research site, Lena River delta, northern Siberia: an opportunity to validate remote-sensing data and land surface, snow, and permafrost models, Earth System Science Data, 11, 261-299, <https://doi.org/10.5194/essd-11-261-2019>, 2019.

Gruber, S., and Haeberli, W.: Permafrost in steep bedrock slopes and its temperature-related destabilization following climate change, Journal of Geophysical Research, 112, <https://doi.org/10.1029/2006jf000547>, 2007.

Guo, D., and Sun, J.: Permafrost Thaw and Associated Settlement Hazard Onset Timing over the Qinghai-Tibet Engineering Corridor, International Journal of Disaster Risk Science, 6, 347-358, <https://doi.org/10.1007/s13753-015-0072-3>, 2015.

Han, F., Yu, W., Zhang, X., Yu, F., Yi, X., and Hu, D.: Parameter sensitivity analyses of influence on thermal regime of embankment in Permafrost Regions along the Qinghai-Tibet Engineering Corridor, Cold Regions Science and Technology, 166, <https://doi.org/10.1016/j.coldregions.2019.102817>, 2019.

Huggel, C., Salzmann, N., Allen, S., Caplan-Auerbach, J., Fischer, L., Haeberli, W., Larsen, C., Schneider, D., and Wessels, R.: Recent and future warm extreme events and high-mountain slope stability, Philosophical Transactions of the Royal Society A: Mathematical, Physical and Engineering Sciences, 368, 2435-2459, <https://doi.org/10.1098/rsta.2010.0078>, 2010.

- Jin, H.-j., Yu, Q.-h., Wang, S.-l., and Lü, L.-z.: Changes in permafrost environments along the Qinghai–Tibet engineering corridor induced by anthropogenic activities and climate warming, *Cold Regions Science and Technology*, 53, 317–333, <https://doi.org/10.1016/j.coldregions.2007.07.005>, 2008.
- Léger, E., Dafflon, B., Robert, Y., Ulrich, C., Peterson, J. E., Biraud, S. C., Romanovsky, V. E., and Hubbard, S. S.: A distributed temperature profiling method for assessing spatial variability in ground temperatures in a discontinuous permafrost region of Alaska, *The Cryosphere*, 13, 2853–2867, <https://doi.org/10.5194/tc-13-2853-2019>, 2019.
- Liu, G., Xie, C., Zhao, L., Xiao, Y., Wu, T., Wang, W., and Liu, W.: Permafrost warming near the northern limit of permafrost on the Qinghai–Tibetan Plateau during the period from 2005 to 2017: A case study in the Xidatan area, *Permafrost and Periglacial Processes*, <https://doi.org/10.1002/ppp.2089>, 2020.
- Luo, L., Ma, W., Zhang, Z., Zhuang, Y., Zhang, Y., Yang, J., Cao, X., Liang, S., and Mu, Y.: Freeze/Thaw-Induced Deformation Monitoring and Assessment of the Slope in Permafrost Based on Terrestrial Laser Scanner and GNSS, *Remote Sens-Basel*, 9, <https://doi.org/10.3390/rs9030198>, 2017.
- Luo, L., Ma, W., Zhao, W., Zhuang, Y., Zhang, Z., Zhang, M., Ma, D., and Zhou, Q.: UAV-based spatiotemporal thermal patterns of permafrost slopes along the Qinghai–Tibet Engineering Corridor, *Landslides*, 15, 2161–2172, <https://doi.org/10.1007/s10346-018-1028-7>, 2018a.
- Luo, L., Ma, W., Zhuang, Y., Zhang, Y., Yi, S., Xu, J., Long, Y., Ma, D., and Zhang, Z.: The impacts of climate change and human activities on alpine vegetation and permafrost in the Qinghai-Tibet Engineering Corridor, *Ecol Indic*, 93, 24–35, <https://doi.org/10.1016/j.ecolind.2018.04.067>, 2018b.
- Luo, L., Zhang, Z., Ma, W., Yi, S., and Zhuang, Y.: PIC v1.3: comprehensive R package for computing permafrost indices with daily weather observations and atmospheric forcing over the Qinghai–Tibet Plateau, *Geosci Model Dev*, 11, 2475–2491, <https://doi.org/10.5194/gmd-11-2475-2018>, 2018c.
- Luo, L., Ma, W., Zhang, Z., Zhuang, Y., Yang, J., Cao, X., Liang, S., and Yi, S.: Integration of terrestrial laser scanning and soil sensors for deformation and hydrothermal monitoring of frost mounds, *Measurement*, 131, 513–523, <https://doi.org/10.1016/j.measurement.2018.09.020>, 2019.
- Luo, L., Zhuang, Y., Zhang, M., Zhang, Z., Ma, W., Zhao, W., Zhao, L., Wang, L., Shi, Y., Zhang, Z., Duan, Q., Tian, D., and Zhou, Q.: TLS measurements in the Qinghai-Tibet Engineering Corridor, <https://doi.org/10.5281/zenodo.3764502>, 2020a.
- Luo, L., Zhuang, Y., Zhang, M., Zhang, Z., Ma, W., Zhao, W., Zhao, L., Wang, L., Shi, Y., Zhang, Z., Duan, Q., Tian, D., and Zhou, Q.: UAV RGB and TIR images in the Qinghai-Tibet Engineering Corridor, <https://doi.org/10.5281/zenodo.3764280>, 2020b.
- Luo, L., Zhuang, Y., Zhang, M., Zhang, Z., Ma, W., Zhao, W., Zhao, L., Wang, L., Shi, Y., Zhang, Z., Duan, Q., Tian, D., and Zhou, Q.: R code of permafrost indices in the Qinghai-Tibet Engineering Corridor, <https://doi.org/10.5281/zenodo.3766712>, 2020c.

- 560 Luo, L., Zhuang, Y., Zhang, M., Zhang, Z., Ma, W., Zhao, W., Zhao, L., Wang, L., Shi, Y., Zhang, Z., Duan, Q., Tian, D., and Zhou, Q.: Meteorological and ground observations in the Qinghai-Tibet Engineering Corridor, <https://doi.org/10.5281/zenodo.3764273>, 2020d.
- Ma, W., Niu, F., Akagawa, S., and Jin, D.: Slope instability phenomena in permafrost regions of Qinghai-Tibet Plateau, China, *Landslides*, 3, 260-264, <https://doi.org/10.1007/s10346-006-0045-0>, 2006.
- 565 Ma, W., Mu, Y., Xie, S., Mao, Y., and Chen, D.: Thermal-mechanical Influences and Environmental Effects of Expressway Construction on the Qinghai-Tibet Permafrost Engineering Corridor, *Advances in Earth Science*, 32, 2017.
- Ma, W., Mu, Y., Zhang, J., Yu, W., Zhou, Z., and Chen, T.: Lateral thermal influences of roadway and railway embankments in permafrost zones along the Qinghai-Tibet Engineering Corridor, *Transportation Geotechnics*, 21, <https://doi.org/10.1016/j.trgeo.2019.100285>, 2019.
- 570 Mu, Y., Ma, W., Li, G., Niu, F., Liu, Y., and Mao, Y.: Impacts of supra-permafrost water ponding and drainage on a railway embankment in continuous permafrost zone, the interior of the Qinghai-Tibet Plateau, *Cold Regions Science and Technology*, 154, 23-31, <https://doi.org/10.1016/j.coldregions.2018.06.007>, 2018.
- Niu, F., Luo, J., Lin, Z., Fang, J., and Liu, M.: Thaw-induced slope failures and stability analyses in permafrost regions of the Qinghai-Tibet Plateau, China, *Landslides*, 13, 55-65, <https://doi.org/10.1007/s10346-014-0545-2>, 2015.
- 575 Obu, J., Westermann, S., Bartsch, A., Berdnikov, N., Christiansen, H. H., Dashtseren, A., Delaloye, R., Elberling, B., Etzelmüller, B., Kholodov, A., Khomutov, A., Kääb, A., Leibman, M. O., Lewkowicz, A. G., Panda, S. K., Romanovsky, V., Way, R. G., Westergaard-Nielsen, A., Wu, T., Yamkhin, J., and Zou, D.: Northern Hemisphere permafrost map based on TTOP modelling for 2000–2016 at 1 km² scale, *Earth-Science Reviews*, 193, 299-316, <https://doi.org/10.1016/j.earscirev.2019.04.023>, 2019.
- 580 Patton, A. I., Rathburn, S. L., and Capps, D. M.: Landslide response to climate change in permafrost regions, *Geomorphology*, 340, 116-128, <https://doi.org/10.1016/j.geomorph.2019.04.029>, 2019.
- Sluijs, J., Kokelj, S., Fraser, R., Tunnicliffe, J., and Lacelle, D.: Permafrost Terrain Dynamics and Infrastructure Impacts Revealed by UAV Photogrammetry and Thermal Imaging, *Remote Sens-Basel*, 10, <https://doi.org/10.3390/rs10111734>, 2018.
- 585 Streletskiy, D. A., Suter, L. J., Shiklomanov, N. I., Porfiriev, B. N., and Eliseev, D. O.: Assessment of climate change impacts on buildings, structures and infrastructure in the Russian regions on permafrost, *Environ Res Lett*, 14, <https://doi.org/10.1088/1748-9326/aaf5e6>, 2019.
- Wang, K., Jafarov, E., Overeem, I., Romanovsky, V., Schaefer, K., Clow, G., Urban, F., Cable, W., Piper, M., Schwalm, C., Zhang, T., Kholodov, A., Sousanes, P., Loso, M., and Hill, K.: A synthesis dataset of permafrost-affected soil thermal conditions for Alaska, USA, *Earth System Science Data*, 10, 2311-2328, <https://doi.org/10.5194/essd-10-2311-2018>, 2018.
- 590 Wang, S., Niu, F., Chen, J., and Dong, Y.: Permafrost research in China related to express highway construction, *Permafrost and Periglacial Processes*, 31, 406-416, <https://doi.org/10.1002/ppp.2053>, 2020.

- Weber, S., Beutel, J., Da Forno, R., Geiger, A., Gruber, S., Gsell, T., Hasler, A., Keller, M., Lim, R., Limpach, P., Meyer, M., Talzi, I., Thiele, L., Tschudin, C., Vieli, A., Vonder Mühll, D., and Yücel, M.: A decade of detailed observations (2008–2018) in steep bedrock permafrost at the Matterhorn Hörnligrat (Zermatt, CH), Earth System Science Data, 11, 1203–1237, <https://doi.org/10.5194/essd-11-1203-2019>, 2019.
- Wicky, J., and Hauck, C.: Numerical modelling of convective heat transport by air flow in permafrost talus slopes, The Cryosphere, 11, 1311–1325, <https://doi.org/10.5194/tc-11-1311-2017>, 2017.
- Wirz, V., Geertsema, M., Gruber, S., and Purves, R. S.: Temporal variability of diverse mountain permafrost slope movements derived from multi-year daily GPS data, Mattertal, Switzerland, Landslides, 13, 67–83, <https://doi.org/10.1007/s10346-014-0544-3>, 2015.
- Wu, Q., Liu, Y., Zhang, J., and Tong, C.: A review of recent frozen soil engineering in permafrost regions along Qinghai-Tibet Highway, China, Permafrost and Periglacial Processes, 13, 199–205, <https://doi.org/10.1002/ppp.420>, 2002.
- Wu, Q., Dong, X., Liu, Y., and Jin, H.: Responses of Permafrost on the Qinghai-Tibet Plateau, China, to Climate Change and Engineering Construction, Arctic, Antarctic, and Alpine Research, 39, 682–687, [https://doi.org/10.1657/1523-0430\(07-508\)\[wu\]2.0.Co;2](https://doi.org/10.1657/1523-0430(07-508)[wu]2.0.Co;2), 2007.
- Wu, Q., and Zhang, T.: Recent permafrost warming on the Qinghai-Tibetan Plateau, Journal of Geophysical Research, 113, <https://doi.org/10.1029/2007jd009539>, 2008.
- Wu, Y., Yang, Q., Jiang, G., and Zhang, P.: Stable Isotopic Stratification and Growth Patterns of Ground Ice in Permafrost on the Qinghai-Tibet Plateau, China, Permafrost and Periglacial Processes, 28, 119–129, <https://doi.org/10.1002/ppp.1892>, 2017.
- Yang, Y., Wu, Q., Jiang, G., and Zhang, P.: Stable Isotopic Stratification and Growth Patterns of Ground Ice in Permafrost on the Qinghai-Tibet Plateau, China, Permafrost and Periglacial Processes, 28, 119–129, <https://doi.org/10.1002/ppp.1892>, 2017.
- Yu, W., Zhang, T., Lu, Y., Han, F., Zhou, Y., and Hu, D.: Engineering risk analysis in cold regions: State of the art and perspectives, Cold Regions Science and Technology, 171, <https://doi.org/10.1016/j.coldregions.2019.102963>, 2020.
- Yuan, C., Yu, Q., You, Y., and Guo, L.: Deformation mechanism of an expressway embankment in warm and high ice content permafrost regions, Appl Therm Eng, 121, 1032–1039, <https://doi.org/10.1016/j.applthermaleng.2017.04.128>, 2017.
- Zhang, M., Pei, W., Zhang, X., and Lu, J.: Lateral thermal disturbance of embankments in the permafrost regions of the Qinghai-Tibet Engineering Corridor, Natural Hazards, 78, 2121–2142, <https://doi.org/10.1007/s11069-015-1823-6>, 2015.
- Zhang, T., Barry, R. G., Knowles, K., Heginbottom, J. A., and Brown, J.: Statistics and characteristics of permafrost and ground-ice distribution in the Northern Hemisphere¹, Polar Geography, 23, 132–154, <https://doi.org/10.1080/10889379909377670>, 1999.
- Zhang, Z., Yu, Q., You, Y., Guo, L., Wang, X., Liu, G., and Wu, G.: Cooling effect analysis of temperature-controlled ventilated embankment in Qinghai-Tibet testing expressway, Cold Regions Science and Technology, 173, <https://doi.org/10.1016/j.coldregions.2020.103012>, 2020.

Zhao, L., Zou, D., Hu, G., Du, E., Pang, Q., Xiao, Y., Li, R., Sheng, Y., Wu, X., Sun, Z., Wang, L., Wang, C., Ma, L., Zhou, H., and Liu, S.: Changing climate and the permafrost environment on the Qinghai–Tibet (Xizang) plateau, Permafrost and Periglacial Processes, 31, 396-405, <https://doi.org/10.1002/ppp.2056>, 2020.

设计
设计
设计